minerals

Article

Late Cryogenian Circum-Rodinia Syn-Subduction Extension: Insights from Highly Fractionated S-Type and A-Type Granitoids in the Northern Tarim Craton

Talifeng Biedilihan [1,†], Nijiati Abuduxun [1,*,†], Peng Huang [2], Jingmin Gan [2] and Yilidan'na Talati [1]

1 Xinjiang Key Laboratory for Geodynamic Processes and Metallogenic Prognosis of the Central Asian Orogenic Belt, School of Geology and Mining Engineering, Xinjiang University, Urumqi 830046, China
2 Xinjiang Key Laboratory of Mineral Resources and Digital Geology, Xinjiang Research Centre for Mineral Resources, Chinese Academy of Sciences, Urumqi 830011, China
* Correspondence: nijatuy@xju.edu.cn
† These authors contributed equally to this work.

Abstract: Late Cryogenian–Ediacaran magmatism represents the latest Precambrian tectonothermal event in the Tarim Craton. However, its geodynamic setting and geological significance are controversial. Here, we report the geochronology, whole-rock geochemistry, and Sr-Nd-Hf isotopic compositions of newly identified late Cryogenian A-type and highly fractionated S-type granites from two locations in the northern Tarim Craton. LA-ICP-MS zircon U-Pb analyses yield ages of 642 ± 7 Ma for a syenogranite and 643 ± 4.5 Ma for a mylonitized granite. The syenogranite is weakly peraluminous and shows an A-type granite affinity, as indicated by its high $K_2O + Na_2O$ contents (8.35–8.64 wt.%), high field strength elements (Zr + Nb + Ce + Y = $435.8 - 463.4 \times 10^{-6}$), Ga/Al ratios (2.79−2.83), and zircon saturation temperatures (829–844 °C). In contrast, the mylonitized granite contains Al-oversaturated minerals (e.g., garnet) and has high a differentiation index (DI = of 98.9–99.4), with lower zircon saturation temperatures (786–792 °C); the samples display high SiO_2 contents (72.99–74.00 wt.%) and A/CNK values (1.16–1.17) and low Nb/Ta and Zr/Hf ratios and are enriched in Rb and depleted in Ba, Sr, which all point to a highly fractionated S-type granite affinity. The granites are characterized by elevated large-ion lithosphere elements (LILEs) and flat high-field-strength elements (HFSEs) patterns, with deep Nb and Ta troughs and pronounced negative Eu anomalies (Eu/Eu* = 0.17–0.38). They show apparently negative $\varepsilon_{Nd}(t)$ values (−10.1 to −9.8 and −6.8 to −7.9, respectively) and $\varepsilon_{Hf}(t)$ values (−9.66 to −1.77 and −33.5 to −1.3, respectively) with Paleoproterozoic crustal model ages, indicating that they were mainly generated by the partial melting of mature crustal materials with a minor contribution from a mantle-derived magmatic source. By integrating with previously published geological, sedimentological, and structural data, we suggest that the granites formed due to a high-temperature gradient in a syn-subduction extensional setting that was probably induced by northward slab rollback of the Paleo-Asian Oceanic lithosphere. Our new data highlight an upper-plate extension in the northern Tarim Craton that constitutes the northern periphery of the Rodinia supercontinent. The linear distribution of late Cryogenian magmatic rocks provides critical evidence for the orogen strike extension of the terminal suture between the Tarim Craton and southwestern Altaids.

Keywords: syn-subduction extension; S-type granite; A-type granite; late Cryogenian; northern Tarim

Citation: Biedilihan, T.; Abuduxun, N.; Huang, P.; Gan, J.; Talati, Y. Late Cryogenian Circum-Rodinia Syn-Subduction Extension: Insights from Highly Fractionated S-Type and A-Type Granitoids in the Northern Tarim Craton. *Minerals* **2023**, *13*, 1446. https://doi.org/10.3390/min13111446

Academic Editor: Jaroslav Dostal

Received: 12 October 2023
Revised: 7 November 2023
Accepted: 8 November 2023
Published: 16 November 2023

1. Introduction

A-type and highly fractionated peraluminous granites have long been the focus of numerous studies because they are generally related to rare-metal mineralization [1,2]. Moreover, A-type granites are widely considered important petrogenetic indicators due to their high melting temperature, which is commonly driven by extensional events [3–5].

Being generated by the partial melting of supracrustal rocks [6], highly fractionated peraluminous granites are not only one of the key indicators of crustal maturity but can also provide critical constraints on crustal anatexis and evolution of continents [7,8].

The Tarim Craton is one of the major Precambrian continental blocks in Asia [9]. It is widely accepted that the Tarim Craton was involved in the assembly and breakup of supercontinent Rodinia in the Neoproterozoic [10,11]. Paleomagnetic data suggest that the Tarim Craton was located in the northwestern periphery of the supercontinent [10–15]. Widespread and diverse magmatism with main episodes of ca. 820–800 Ma and ca.780–750 Ma, as a response to the protracted fragmentation of the Rodinia, have been well-documented in the Tarim Craton [16]. By contrast, less attention has been paid to late Cryogenian–Ediacaran magmatism in the area. As much as 660–600 Ma basaltic and granitic rocks have recently been reported from several locations (e.g., Korla and Aksu) [17–25], representing the latest Precambrian magmatism in the Tarim Craton. However, the geodynamic setting and geological significance of the magmatism remain controversial due to their limited exposure. They were previously interpreted to be formed in the process of (1) post-collisional extension [19,26,27]; (2) plume-induced extension [9,28,29]; and (3) circum-Rodinia subduction [17,30–32].

It is worth noting that the Tarim Craton was probably affected by the long-lasting tectonic evolution of the southern Altaids in the Paleozoic, as a result of which arc-related magmatic rocks were developed in its northern margin [33,34]. Thus, the Paleozoic magmatism is less diagnostic to constrain the boundary between the northern Tarim Craton and the southern Altaids. Therefore, the distribution of the late Neoproterozoic igneous rocks with typical Tarim signatures, which are usually absent in the southern Altaids, can provide key evidence to determine the tectonic boundary between them.

In this contribution, we report LA-ICP-MS zircon U-Pb geochronology, whole-rock geochemistry, and Sr-Nd-Hf isotopic compositions of newly identified late Cryogenian A-type and highly fractionated S-type granites from two locations in the northern Tarim Craton, aiming to constrain their magma source, petrogenesis, and tectonic setting.

2. Geological Setting

The Tarim Craton, one of the three major cratons in China, is surrounded by the southern Altaids to the north, the Western Kunlun orogen to the south, and the Altyn Tagh orogen to the southeast (Figure 1a,b) [9,35]. It covers an area of about 600,000 km^2, with over 90% buried by Quaternary sediments. Precambrian basement rocks representing early thermotectonic events in the Tarim Craton are exposed only along its marginal blocks due to the extensive coverage of desert or Cenozoic sedimentary rocks (Figure 1b) [9,17,30]. The northern Tarim Craton comprises two major lithological units: the crystalline basement and the overlying sedimentary cover. The former includes Archean tonalite-trondhjemite–granodiorite (TTG) gneiss and granitoids (ca. 2.8–2.5 Ga) with amphibolite and paragneiss enclaves (2.65–2.51 Ga), early Paleoproterozoic orthogneiss (2.47–2.46 Ga and 2.36–2.29 Ga), late Paleoproterozoic granitoids (1.94–1.93 Ga), and metamorphosed supracrustal sequences (2.0–1.85 Ga) [17,36,37]. These basement rocks underwent upper amphibolite to granulite facies metamorphism in the late Paleoproterozoic (1.9–1.8 Ga) [38], and are unconformably overlain by low-grade late Mesoproterozoic to early Neoproterozoic metasedimentary and volcanic successions [39] and by middle Neoproterozoic high-pressure metamorphic rocks [40]. Late Neoproterozoic rift-related shallow marine clastic and carbonate rocks, glacial diamictite, and bimodal volcanic rocks [28,41,42], which were previously ascribed to the Quruqtagh Group [43], are well-exposed along the northern Tarim. The northern Tarim hosts diverse Neoproterozoic magmatic rocks, including (1) 830–735 Ma and 660–630 Ma granitoids [17,37]; (2) ~800 Ma mafic-ultramafic-carbonatite complexes [44]; (3) 760 Ma and 735 Ma bimodal intrusive complexes [45], and (4) 820 Ma, 780–770 Ma and 660–630 Ma mafic dyke swarms [23,46]. The Neoproterozoic extensive magmatism and metamorphism in the Tarim Craton were previously proposed to be global-scale tectonothermal events related to the assembly and breakup of Rodinia [16,30].

The South Tianshan is bounded by the Atbashi–Inylchek–Kawabulak Fault to the north and the North Tarim Fault to the South (Figure 1b) [47] and constitutes the southwest end of the Altaids, which is one of the largest accretionary orogens on Earth [48,49]. It grew as a result of the consumption of the South Tianshan Ocean, followed by its final collision with the northern Tarim Craton [50,51], and consequently, it contains key records of terminal suturing between the Altaids and the Tarim Craton [47,52,53]. The South Tianshan is predominantly composed of Paleozoic and Mesozoic sedimentary rocks, Paleozoic ophiolites, (ultra-)-high-pressure eclogites, blueschists, and granulites [53–56]. Paleozoic magmatic rocks are distributed discontinuously along the South Tianshan [57,58].

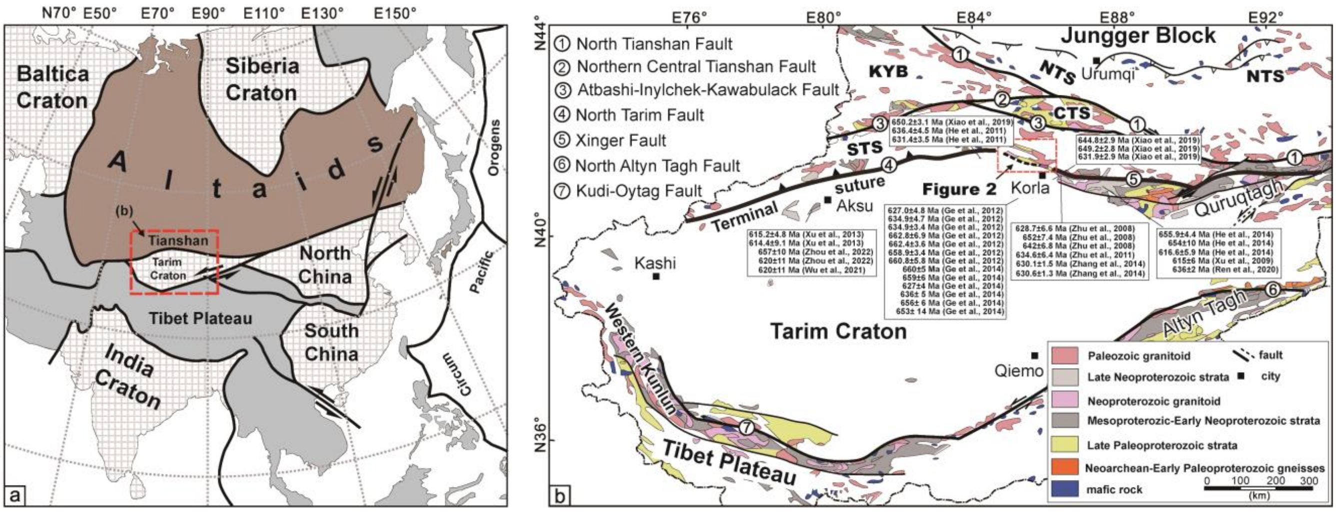

Figure 1. (**a**) Simplified tectonic map showing the Altaids and surrounding cratons (modified after [48]). The position of (**b**) is marked. (**b**) Sketch map of the Tarim Craton and adjacent areas in northwestern China (modified after [17]) showing spatial and temporal distributions of compiled crystallization ages of late Cryogenian–Ediacaran magmatism (see Supplementary Table S1 for details and data sources). The position of the terminal suture between the Altaids and the Tarim Craton is according to [52]. The position of Figure 2 is marked. Abbreviations: NTS—North Tianshan; CTS—Central Tianshan; STS—South Tianshan; KYB—Kazakhstan-Yili Block. Literature data are from [17–19,22–24,28–32].

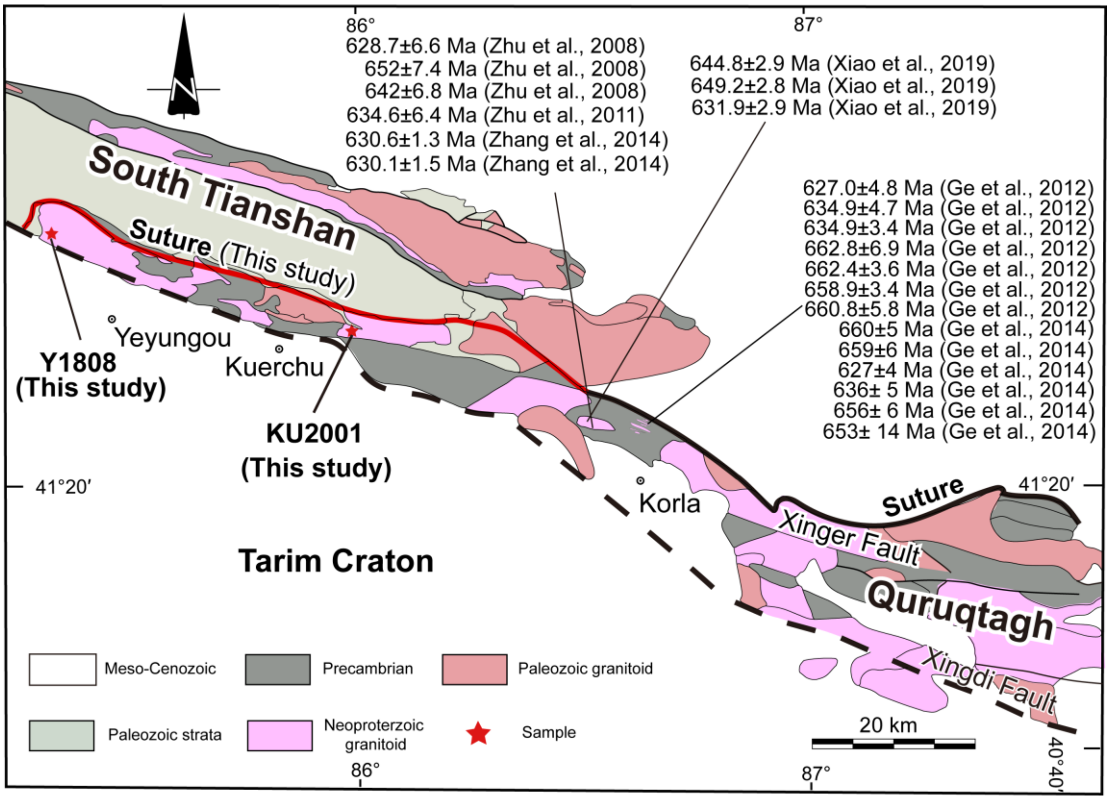

Figure 2. Simplified geological map of the Ku'erchu and Yeyungou area in the northern Tarim Craton showing sampling sites and distribution of late Cryogenian–Ediacaran granitoids (see Supplementary Table S1 for details and data sources). The tectonic boundary (thick black line) between the South Tianshan and Quruqtagh is according to [51]. Its western extension, proposed in this study, is marked with a thick red line. The dashed line represents the previously proposed position of the suture [50]. Literature data are from [17,18,23–25,29].

3. Sampling and Analytical Methods

Intrusive rocks are widely exposed along the Ku'erchu and Yeyungou areas in the northern Tarim and are dominantly composed of granitoids (Figure 2). Samples for zircon U-Pb dating, Lu-Hf-isotopes, and whole rock geochemical and Sr-Nd isotopic analysis were collected from two plutons as shown in Figure 2. Sample KU2001 was collected from a coarse-grained pinkish syenogranite in the Ku'erchu area (Figure 2). Sample Y1808 was collected from a grey mylonitized granite exposed northwest of Yeyungou village (Figure 2). Data acquisition and detailed analytical procedures for the samples are presented in Supporting Information (Text S1).

4. Sample Description and Brief Petrography

The syenogranite (KU2001) has intruded a paragneiss of the Palaeoproterozoic Xingditagh group (Figure 3a,c). As shown in Figure 3f, it mainly consists of alkali feldspar (55%–60%), plagioclase (10%–15%), quartz (20%–25%), and minor biotite (3%–5%). Accessory minerals include zircon and apatite.

The mylonitized granite (Y1808) is overlain by an unmetamorphosed sandstone that was previously ascribed to the early Carboniferous Yeyungou Group (Figure 3b) [43]. The granite was mylonitized, as indicated by δ-type residual spots of plagioclase (Figure 3d), mylonitic foliation (Figure 3e), and the elongated quartz grains (Figure 3g). As shown in Figure 3g,h, the granite contains microcline (50%–55%), perthite (~5%), plagioclase (5%–10%), quartz (20%–25%), biotite (2%–3%), and muscovite (2%–3%). The sample contains garnet (Figure 3h).

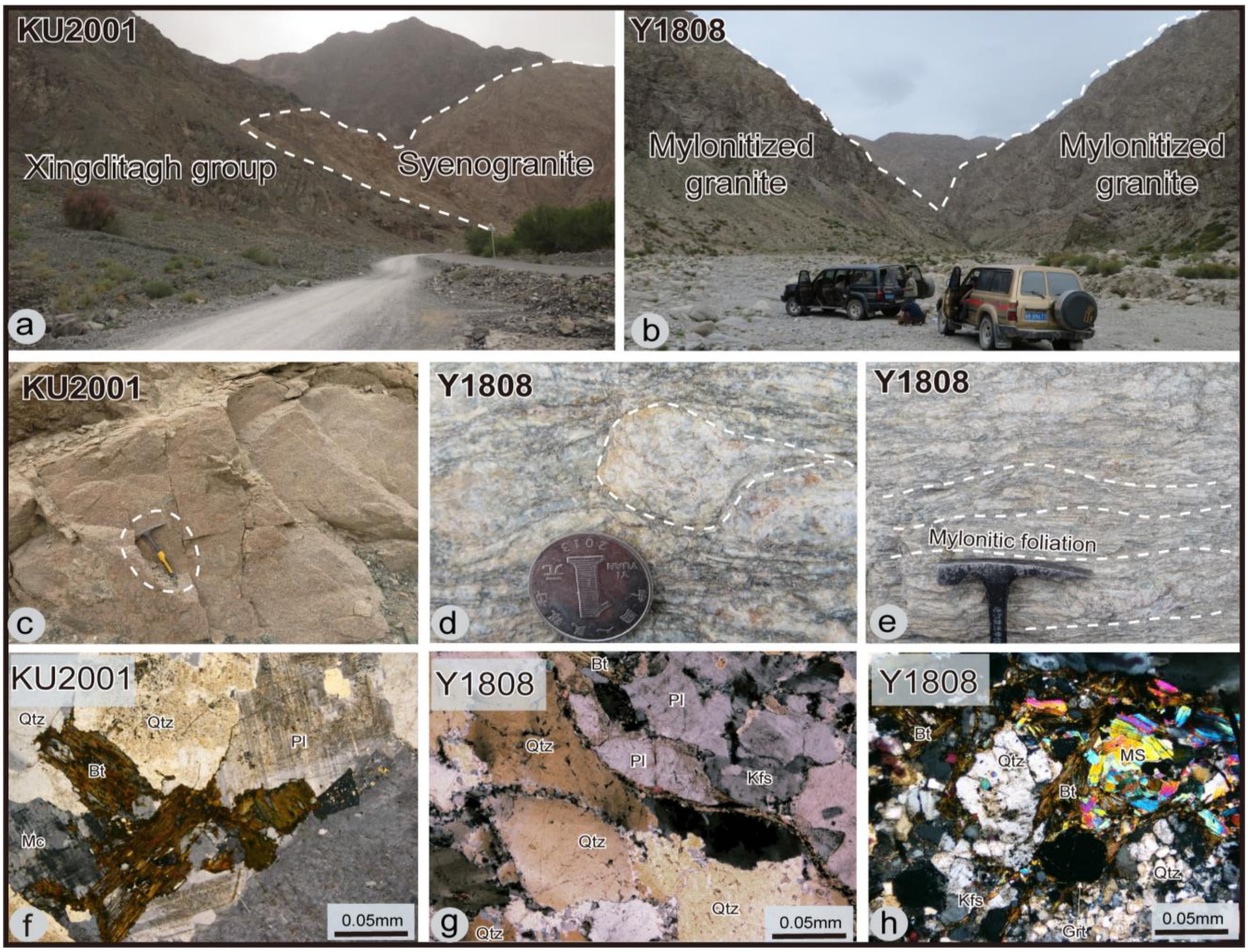

Figure 3. (**a**) A field photo showing that the syenogranite intruded Xingditagh Group in the Ku'erchu area. (**b**,**c**) Field photos showing outcrops and field occurrences of the mylonitized granite and syenogranite. (**d**) A σ-type porphyroclast of plagioclase. (**e**) Mylonitic foliation in the granite. (**f**) Main mineral compositions of the syenogranite. (**g**) Ductile deformation of quartz grains in the mylonitized granite. (**h**) Main mineral compositions of the granitic mylonite showing the presence of Al-oversaturated minerals such as garnet. Abbreviations: Qtz—Quartz; Bt—Biotite; Grt—Garnet; Pl—Plagioclase; Mc—Microcline; Ms—Muscovite; Kfs—K-feldspar.

5. Results

5.1. Zircon U-Pb Ages and Hf Isotopes

The results of zircon U-Pb dating and in situ Lu-Hf isotopes are listed in Supplementary Table S2 and Supplementary Table S3, respectively.

The cathodoluminescence (CL) images (Figure 4) show that zircons separated from the samples are colorless, transparent to semi-transparent, predominantly euhedral and prismatic, up to 150–300 μm long, and with aspect ratios of 1:1–1:3. The grains display clear oscillatory zoning, and mostly have high Th/U ratios (0.3–1.92), indicating a magmatic origin [59].

A total of eighteen analyses of the syenogranite sample KU2001 yield concordant ages between 620 and 691 Ma and define a weighted mean $^{206}Pb/^{238}U$ age of 642 ± 7 Ma (MSWD = 3.5) (Figure 5a). This age is interpreted to be the crystallization age of sample KU2001. All eighteen spots were analyzed for their Hf isotopic compositions. The data show negative $\varepsilon_{Hf}(t)$ values of −1.8 to −9.7 (Figure 6), with corresponding crustal model ages (T_{DM2}) between 1684 and 2196 Ma (Figure 7).

Figure 4. Representative cathodoluminescence (CL) images showing the internal structure of zircons. The U-Pb (solid red circles) and Hf (yellow dashed circles) analytical sites are marked, and the corresponding numbers refer to the analytical results.

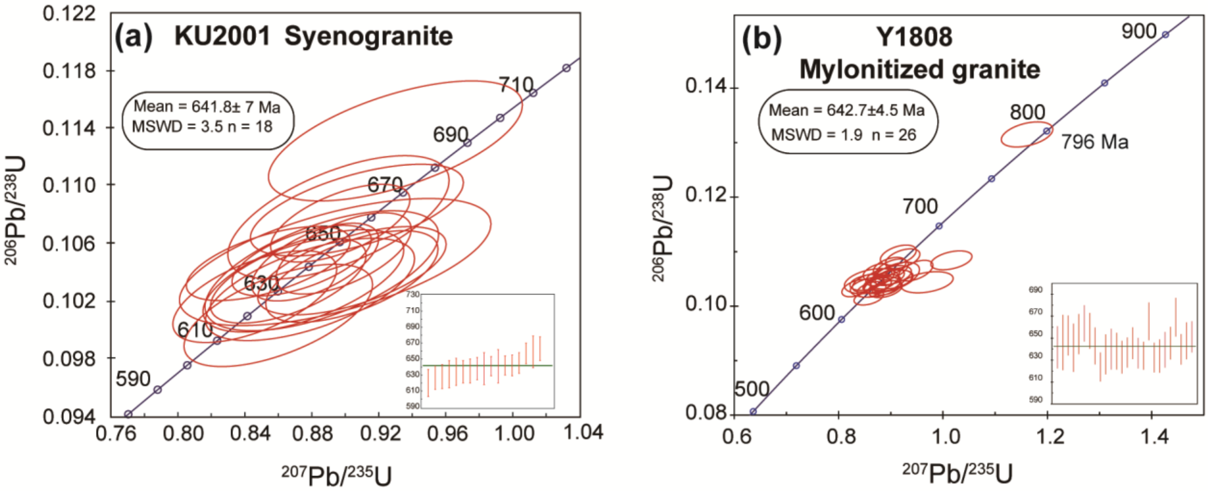

Figure 5. U-Pb Concordia diagrams of zircons from the studied granites. Ages are in Ma and ellipses show 1σ errors.

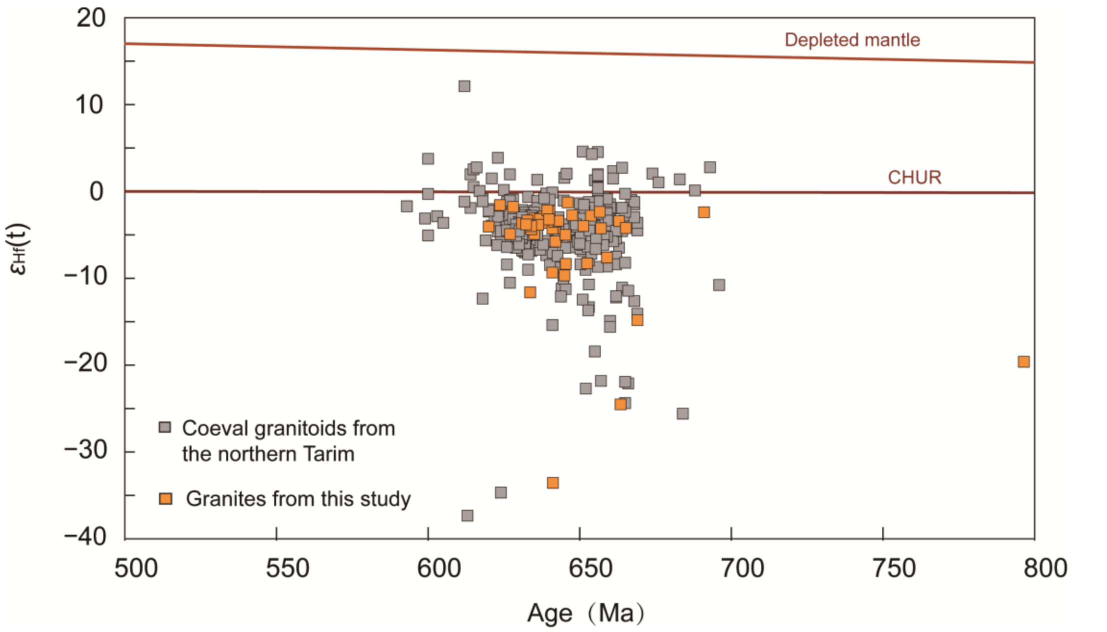

Figure 6. Crystallization age versus ε_{Hf} (t) diagram for igneous zircons from the studied granites in the northern Tarim. Literature data are from [17,18,20,21,25,29].

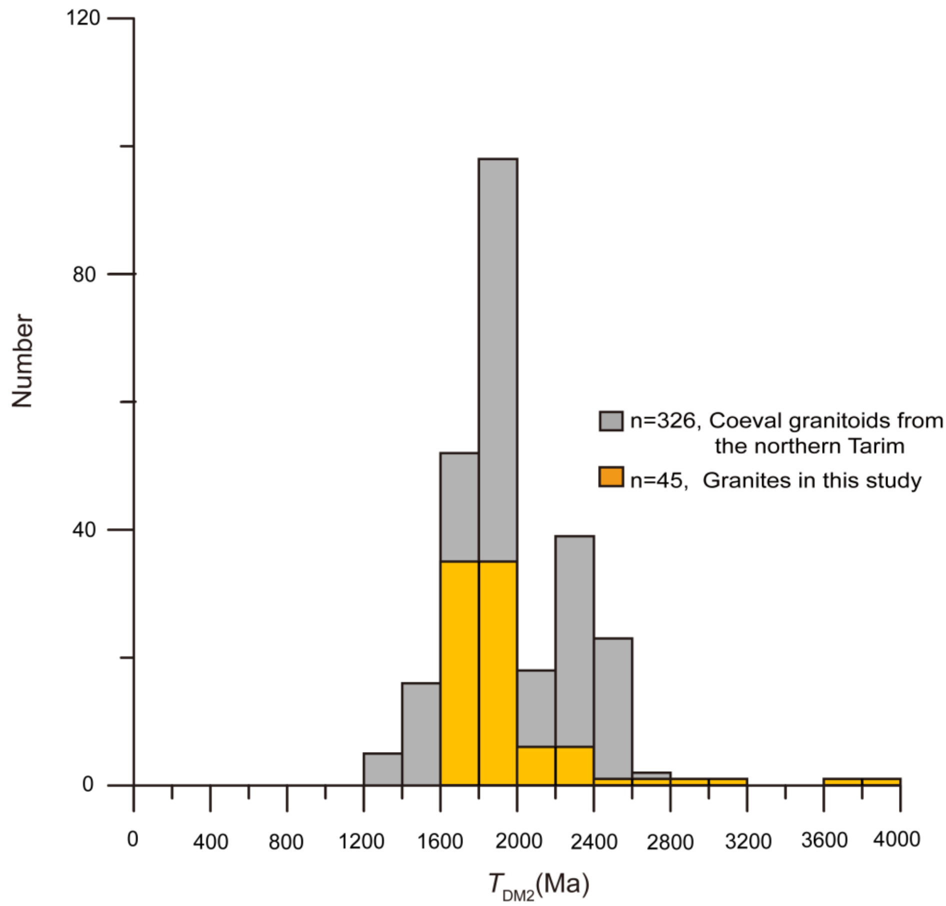

Figure 7. Histograms of crustal Hf model age (T_{DM2}) versus crystallization age of zircons from the studied granites in the northern Tarim. Literature data are from [17,18,20,21,25,29].

Out of the thirty analyses of the mylonitized granite sample Y1808, three were performed on the inherited or captured zircons with prominent older ages of 1810 ± 25 Ma, 1248 ± 19 Ma, and 796 ± 11 Ma (Y1808-1, Y1808-4, and Y1808-28, respectively). One spot (Y1808-12) provides a slightly younger age (573 Ma), probably due to radiogenic Pb loss. The remaining twenty-six analyses yield a weighted mean $^{206}Pb/^{238}U$ age of 643 ± 4.5 Ma (MSWD = 1.9) (Figure 5b) representing the crystallization age of sample Y1808. Twenty-six spots on the dated zircons were analyzed for their Hf isotopic compositions. Twenty-two grains display $\varepsilon_{Hf}(t)$ values ranging from −11.6 to −1.25 (Figure 6), corresponding to T_{DM2} ages between 1666 and 2310 Ma (Figure 7). The other four zircons (Y1808-6, Y1808-8, Y1808-26, and Y1808-28, respectively) show more negative $\varepsilon_{Hf}(t)$ values of −33.5, −24.5, −14.8, and −19.6, with corresponding older T_{DM2} ages of 3.68, 3.13, 2.53, and 2.93 Ga, respectively.

5.2. Whole Rock Geochemistry

The results of major and trace element geochemical analyses of the studied granites are listed in Supplementary Table S4. All samples display very low values of loss on ignition (LIO < 1.0), indicating that the affection of post-magmatic alteration on the compositions of the granites is limited.

All samples generally show high SiO_2 contents ranging from 72.99 to 74.10 wt.% and total alkali ($K_2O + Na_2O$) contents between 7.57 and 8.64 wt.%, and they plot in the granite field in the SiO_2 (wt.%) versus ($K_2O + Na_2O$) (wt.%) classification diagram for plutonic rocks (Figure 8a). These samples are characterized by moderate contents of Al_2O_3 (13.02–13.85 wt.%) and by low concentrations of TiO_2 (0.18–0.27 wt.%), CaO (0.76–0.95 wt.%), MgO (0.24–0.41 wt.%), and P_2O_5 (0.03–0.20 wt.%). They have high K_2O contents ranging from 4.79 to 5.06 wt.% and K_2O/Na_2O ratios from 1.36 to 1.72 (Supplementary Table S4). All samples fall into the high-K calc-alkaline area in the SiO_2 (wt.%) versus K_2O (wt.%) diagram (Figure 8b). Sample KU2001 shows relatively lower A/CNK ratios ranging from 1.02 to 1.05, suggesting a weakly peraluminous affinity (Figure 8c). In contrast, sample Y1808 is strongly peraluminous (Figure 8c), as indicated by its high A/CNK ratios (1.16–1.17).

All samples show similar chondrite-normalized rare earth element (REE) patterns, as indicated by their significant enrichments in light rare earth elements (LREEs) relative to heavy rare earth elements (HREEs) with La_N/Yb_N ratios between 4.98 and 19.74 (Figure 9a). The high $(La/Sm)_N$ ratios (4.57–7.87) indicate a significant fractionation of REEs. They show distinct negative Eu anomalies (Eu/Eu* = 0.17–0.38) with a concave upward shape (Figure 9a).

All samples show conspicuous enrichments of some large ion lithophile elements (LILEs), such as Rb, Th, U, and evident depletion of Nb, Ta, and Sr in the primitive mantle-normalized spider diagrams (Figure 9b).

5.3. Sr-Nd Isotopes

Rb-Sr and Sm-Nd isotopic compositions for six samples are listed in Supplementary Table S5, and the plot of $(^{87}Sr/^{86}Sr)_i$ versus $\varepsilon_{Nd}(t)$ is shown in Figure 10.

Three samples of the syenogranite (KU2001) exhibit $^{87}Sr/^{86}Sr$ ratios ranging from 0.75240 to 0.76284 and $^{143}Nd/^{144}Nd$ ratios from 0.51173 to 0.51177. They have initial $^{87}Sr/^{86}Sr$ ratios of 0.7075–0.7099 and negative age-corrected $\varepsilon_{Nd}(t)$ values between −10.1 and −9.8, with corresponding crustal model ages (T_{DM2}) from 2.14 to 2.16 Ga.

Three samples of the mylonitized granite (Y1808) exhibit $^{87}Sr/^{86}Sr$ ratios ranging from 0.75316 to 0.75369 and $^{143}Nd/^{144}Nd$ ratios from 0.511202 to 0.511204. They show a small range of initial $^{87}Sr/^{86}Sr$ ratios from 0.7097 to 0.7098 and negative age-corrected $\varepsilon_{Nd}(t)$ values of −6.8 to −7.9, with corresponding crustal model ages (T_{DM2}) between 1.90 and 1.98 Ga.

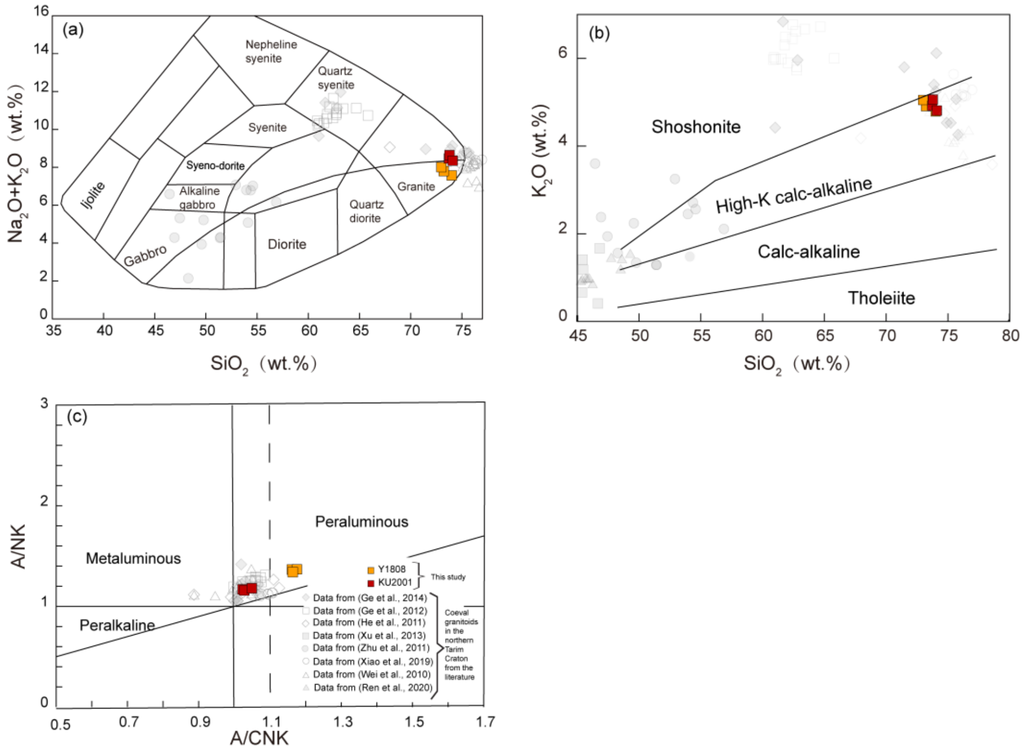

Figure 8. Geochemical classification diagrams of the studied granitoid, and their characteristic major elements. (**a**) SiO_2 (wt.%) versus (K_2O + Na_2O) (wt.%) diagram [60] showing the samples plot in the fields of granite, which is consistent with their main mineral compositions shown in Figure 3. (**b**) SiO_2 (wt.%) versus K_2O (wt.%) diagram [61] showing that the investigated granitoids belong to the high calc-alkaline series. (**c**) Plot of A/CNK (molar Al_2O_3/[CaO + Na_2O + K_2O]) versus A/NK (molar Al_2O_3/[Na_2O + K_2O]) [62] showing the peraluminous to metaluminous nature of the granitoids. Literature data are from [17–19,22,24–26,30].

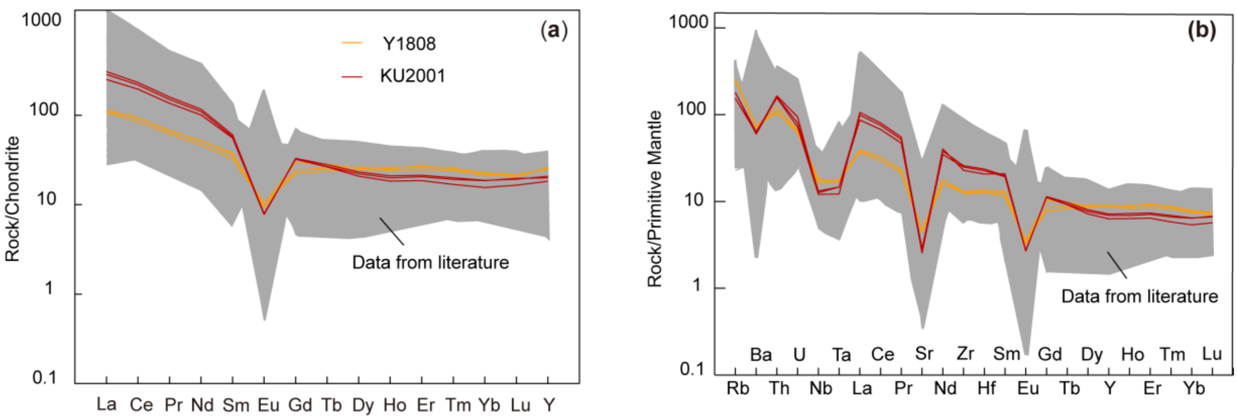

Figure 9. (**a**) Chondrite-normalized REE patterns. (**b**) Primitive mantle-normalized multi-element diagrams. Chondrite and primitive mantle values are from [63]. Literature data are from [17–19,25,26].

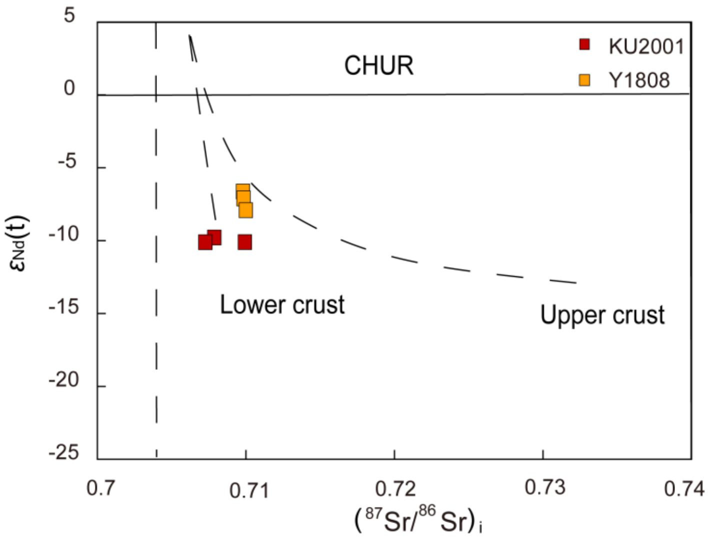

Figure 10. Whole rock initial $^{87}Sr/^{86}Sr$ versus $\varepsilon_{Nd}(t)$ diagram of the studied granites in the northern Tarim.

6. Discussion

6.1. Petrogenetic Classification of the Granites

It is well-accepted that granites are divisible into four sub-types—S-, I-, A-, and M-types—based on their mineralogical and geochemical features [64–66].

The syenogranite (KU2001) displays high SiO_2 (73.73–74.10 wt.%) and total alkali (K_2O + Na_2O = 8.35–8.64 wt.%) contents, with high FeO/MgO ratios. It has lower contents of CaO (0.76–0.88 wt.%) and MgO (0.24–0.28 wt.%). The primitive mantle-normalized spider diagrams are characterized by well-defined positive anomalies of Zr, Ce, Y, and REE, and by significant negative anomalies of Sr, Eu, Ti, and Ba (Figure 9b). All these geochemical characteristics are comparable to that of typical A-type granites [5,67,68]. The samples have higher average Th/U ratios (7.9), which is similar to those of A-type Malani granites [69], In addition, the syenogranite samples show high Ga/Al ratios (2.79–2.83), greater than 2.6, which have been widely accepted as an important parameter for identifying A-type granites [5]. All samples also plot within the A-type granite field in the (Zr + Nb + Ce + Y) (ppm) versus (K_2O+Na_2O) /CaO and (Zr + Nb + Ce + Y) (ppm) versus FeO^T/MgO diagrams (Figure 11c,d). Moreover, the syenogranite samples have high zircon saturation temperatures (829–844 °C), which are much higher than those of I- and S-type granites but consistent with those of typical A-type granites [65,70]. High Zr/Hf ratios (39.58–40) further indicate that the samples are distinctly different from highly fractionated I-type granites [71]. Therefore, we conclude that the syenogranite has an A-type affinity.

The mylonitized granite samples have lower zircon saturation temperatures (786–792 °C) and (Zr + Nb + Ce + Y) contents (244×10^{-6}~256×10^{-6}), which is distinctly different from those of A-type granites. As shown in Figure 3h, the mylonitized granite contains Al-oversaturated minerals, such as muscovite and garnet. Geochemically, the samples show strong peraluminous features, as indicated by their high A/CNK ratios (1.16–1.17) and initial $^{87}Sr/^{86}Sr$ values (0.7092–0.7093), which are similar to those of typical S-type granites [65]. In particular, the mylonitized granite samples have a high differentiation index (DI) of 98.9–99.4, which is consistent with the presence of Al-rich minerals such as garnet (Figure 3h). The samples are enriched in Rb, depleted in Ba and Sr, and show distinct negative Eu anomalies with a concave upward shape (Figure 9a). All these features are very similar to those of highly fractionated peraluminous granites from South China and Central Europe [1,7]. Additionally, all the samples have lower Zr/Hf and Nb/Ta ratios and plot in the highly fractionated field in the Zr/Hf versus Nb/Ta diagram (Figure 11b). They also follow a trend for highly fractionated S-type granites in the major and trace elemental discrimination diagrams (Figure 11c,d). Therefore, we consider that the mylonitized granite to be a highly fractionated S-type granite.

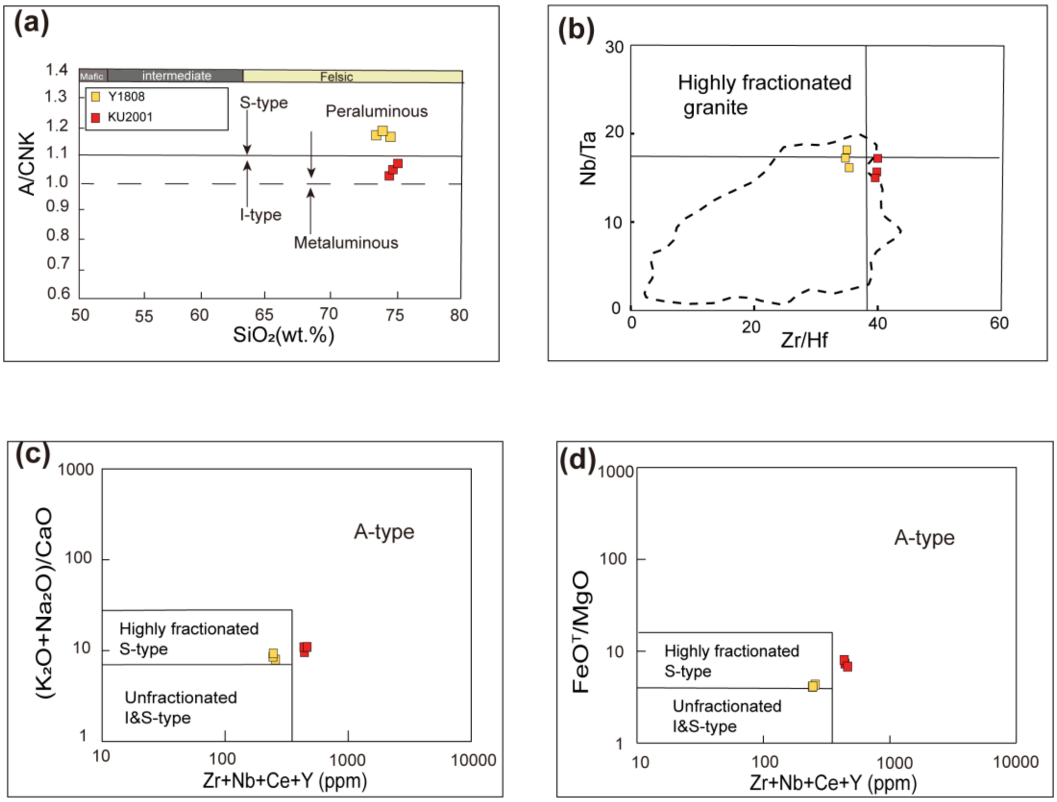

Figure 11. Genetic discrimination diagrams of the studied granites in the northern Tarim. (**a**) SiO_2 (wt.%) versus A/CNK (molar Al_2O_3/[CaO + Na_2O + K_2O]) diagram [62]; (**b**) Zr/Hf versus Nb/Ta diagram [72]; (**c**) (Zr + Nb + Ce + Y) (ppm) versus (K_2O + Na_2O)/CaO; and (**d**) (Zr + Nb + Ce + Y) (ppm) versus FeO^T/MgO diagrams [5].

6.2. Magma Source and Petrogenesis

It is commonly thought that A-type granites are mostly generated due to a high-temperature gradient in extensional settings regardless of their magma source [5,71]. The main petrogenetic models for the origins of A-type granites include: (1) fractionation of mantle-derived magmas [73–75]; (2) partial melting of crustal materials [5,64,76]; and (3) magma mixing between mantle-derived and crustal melts [77,78].

Given the fact that the A-type syenogranite is not associated with coeval mafic-intermediate rocks, it was unlikely directly generated by the differentiation of mantle-derived magmas, which requires extensive fractional crystallization of large volumes of basaltic magmas [70,79–81]. The peraluminous feature of the syenogranite, as indicated by its A/CNK values (1.02–1.04), is distinctly different from those of peralkaline A-type granites from the Lachlan orogen, which were likely produced by fractionation from a mafic source [70,79]. The high SiO_2 (>70 wt.%), low MgO contents (0.24–0.28), and lower $Mg^{\#}$ values (20.7–23.5) of the syenogranite also do not support a mantle origin [64,82,83]. The syenogranite displays negative $\varepsilon_{Hf}(t)$ values (−1.77 to −9.66) and Paleoproterozoic two-stage model ages (1.69–2.20 Ga), which is consistent with their negative $\varepsilon_{Nd}(t)$ values (−9.8 to −10.1) and corresponding crustal model ages (2.14–2.16 Ga), indicating a relatively mature crustal source. This is further supported by the high Rb/Sr ratios (1.67, >0.5) and Th contents (13.3×10^{-6}~14.0×10^{-6}) of the samples [63,84]. The molar oxide discrimination diagrams of CaO/(MgO + FeO^T) vs. Al_2O_3/(MgO + FeO^T) and Rb/Sr vs. Rb/Ba indicate that the syenogranite was likely generated by partial melting of meta-greywackes (Figure 12). The negative Nd-Hf isotopic compositions and inconsiderable variations of their initial ratios contrast with magma mixing between basaltic and crustal melts, which is also supported by the lack of inherited zircons and mafic microgranular enclaves in the syenogranite.

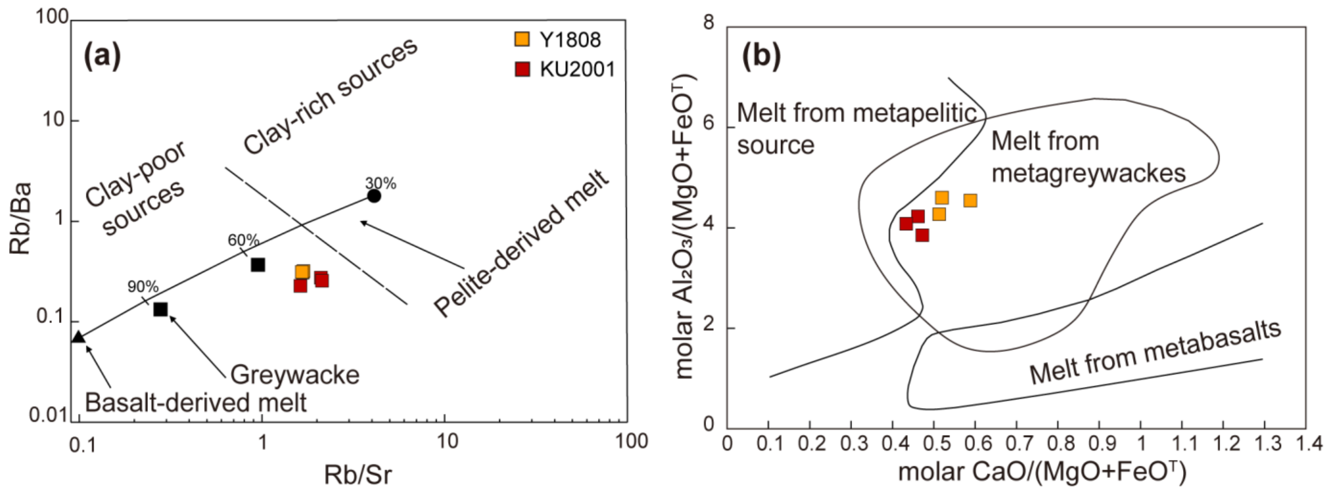

Figure 12. (**a**) Rb/Sr versus Rb/Ba [6] and (**b**) molar CaO/(MgO + FeO^T) versus molar Al_2O_3/(MgO + FeO^T) [85] diagrams for the studied granites in the northern Tarim.

The presence of Al-oversaturated minerals, integrated with the peraluminous affinity of the mylonitized granite, as indicated by its high A/CNK ratios (1.16–1.17) and initial $^{87}Sr/^{86}Sr$ values (0.7092–0.7093), indicate that a significant portion of supracrustal materials was involved in the magma source. The negative $\varepsilon_{Hf}(t)$ and $\varepsilon_{Nd}(t)$ values (−1.77 to −33.54 and −7.9~−6.8, respectively), with the corresponding ancient two-stage model ages, demonstrate a main contribution from Paleoproterozoic to Archean crustal rocks in the Tarim Craton. Both the molar oxide discrimination diagram of CaO/(MgO + FeO^T) versus Al_2O_3/(MgO + FeO^T) and the trace elements discrimination diagram of Rb/Sr versus Rb/Ba indicate that the granites were mainly derived from greywackes (Figure 12).

In summary, several lines of evidence presented above point to the studied late Cryogenian granites probably being generated via the partial melting of mature crustal materials with a minor contribution from a mantle-derived magmatic source.

6.3. Implication for the Late Cryogenian Syn-Subduction Extension in the Northern Tarim

Recent studies have pointed out that late Cryogenian–early Ediacaran magmatism is one of the major tectonothermal events in the Tarim Craton (Figure 1b and references therein). However, no consensus has been reached on the geodynamic setting responsible for the late Cryogenian (600–680 Ma) magmatism in the Tarim Craton. As noted earlier, the existing main models include (1) a result of post-collisional extension [19,26,27]; (2) a single mantle plume model [28,29]; (3) a circum-Rodinia subduction–accretion model [17,18]

The post-collision model proposed that the Mid-Neoproterozoic collision of the Tarim Craton with the Yili-Central Tianshan Terrane was followed by Late Neoproterozoic (Ediacaran) intra-continental extension [27]. However, there are currently no reports of coeval Ediacaran magmatism in the Yili-Central Tianshan Terrane. This implies that the post-collisional extension is unlikely the possible geodynamic setting, in which magmatism generally occurs in both colliding continental blocks. In addition, the tectonic affinity of the Central Tianshan with the Tarim Craton is controversial [86,87], and there are no other geological records that could support such a collision and subsequent separation between them.

The mantle plume model was proposed mainly based on the formation of (1) ca. 800 Ma mafic-ultramafic-carbonatite complex, adakites, and mafic dykes [46]; and (2) 780–760 Ma tholeiitic mafic-ultramafic rock assemblage of coeval basaltic-andesitic-granitic rocks [20], which is a common product of modern Andean-type continental margins. Geochemically, the late Cryogenian magmatism in the Tarim Craton mostly shows arc-related whole-rock geochemical signatures, as indicated by the pronounced negative anomalies of Nb and Ta, elevated LILEs, and flat HFSEs patterns (e.g., Figure 9a,b [19,26,29]), which all are very similar to those of subduction-related magmatic rocks in the Lachlan accretionary orogen in Australia [3]. Accordingly, the granites plot in the volcanic arc field in the trace-element discrimination diagrams (Figure 13). Furthermore, as shown in Figures 6 and 10, the late Cryogenian granitoids were mainly derived from reworking of Archean and/or Paleoproterozoic lower crust with little mantle contribution as indicated by their enriched Nd-Hf isotopic compositions. Most importantly, the late Cryogenian A-type granites in the northern Tarim Craton have an A_2-subtype affinity based on the ternary discrimination diagrams (Figure 14), and that is distinctly different from plume-induced A_1-subtype granites [88], providing critical constraints on the geodynamic setting for the late Cryogenian magmatism in the northern Tarim Craton. The subduction-related setting is also supported by sedimentological studies that have indicated that detrital zircons from the late Cryogenian strata in the northern Tarim Craton fall in the fields of convergent and collisional settings [32].

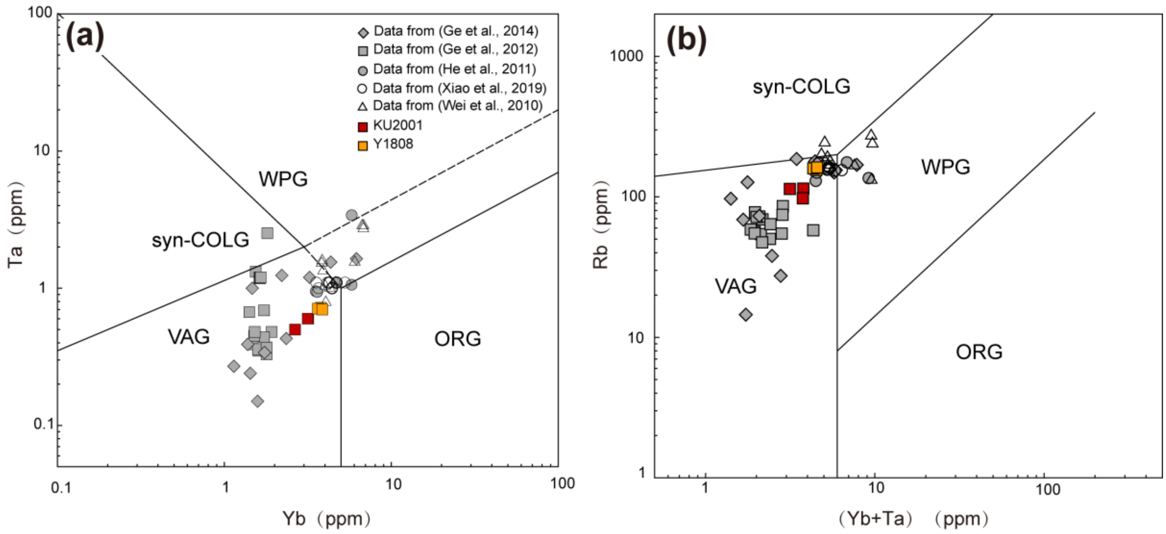

Figure 13. (**a**) Yb (ppm) versus Ta (ppm) diagram [89] and (**b**) (Yb+Ta) (ppm) versus Rb (ppm) diagram [89] showing the volcanic arc origin of the late Cryogenian–early Ediacaran granitoids in the northern Tarim Craton. Literature data are from [17–19,25,26].

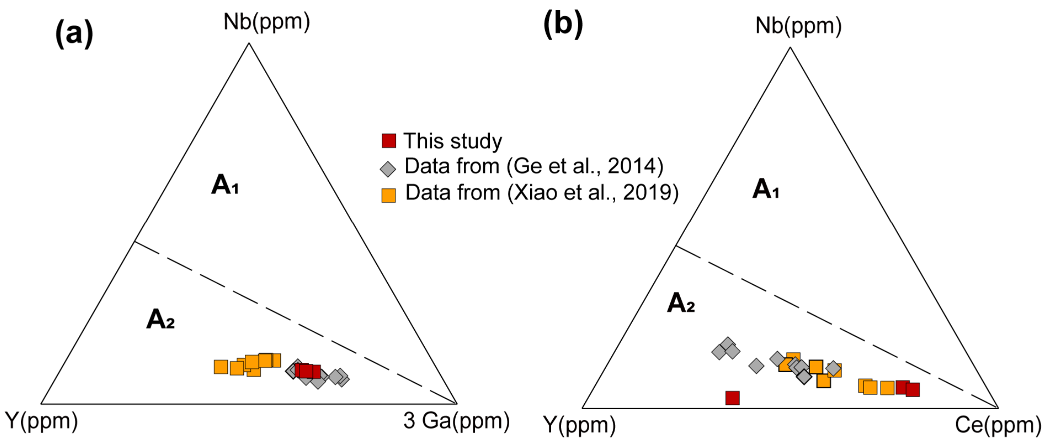

Figure 14. (**a**) Nb-Y-3 Ga and (**b**) Nb-Y-Ce discrimination diagrams [4] show the A_2-subtype affinity of the A-type granites in the northern Tarim Craton. Literature data are from [17,25].

Therefore, by integrating our new data with the evidence presented above, we propose a new petrogenetic-tectonic model as visualized in Figure 15. The late Cryogenian magmatism in the northern Tarim Craton well represents the latest stage of a long-lasting circum-Rodinia subduction system (Figure 15a), which was previously proposed based on voluminous comprehensive geochronological, sedimentological, and structural data [12,30–32,90]. In particular, the presence of A_2-type granites with diagnostic subduction-related geochemical signatures, as reported in this study, requires a high melting temperature, which is widely considered to be associated with extension events in convergent margins [4]. This reasoning indicates an extensional supra-subduction setting along the northern Tarim Craton in the late Neoproterozoic. This reasoning is further supported by the fact that the Ediacaran strata in the northern Tarim Craton show a broad depression related to weak passive rifting [31,91] that is distinctly different from plume-induced intensive active rifting [32,92].

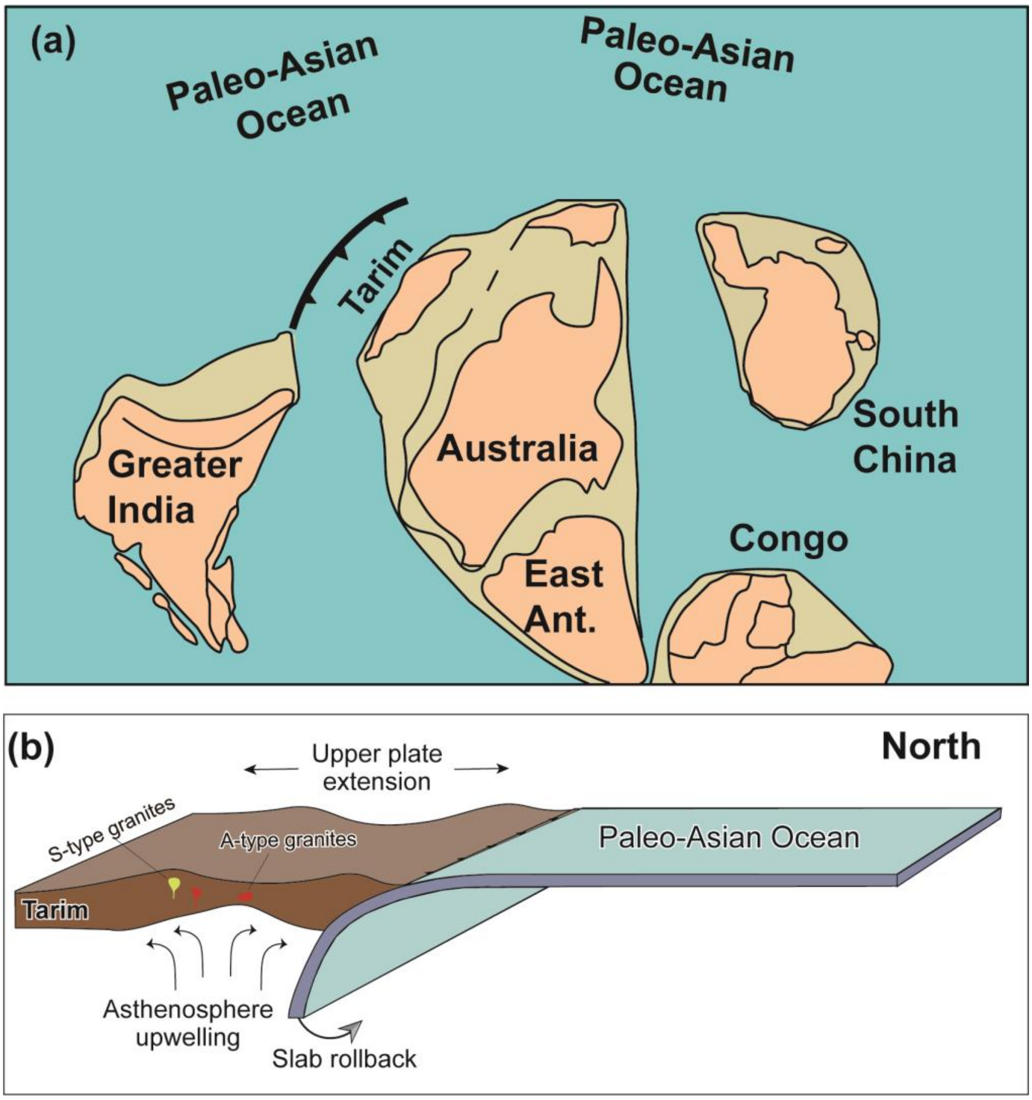

Figure 15. (**a**) A simplified map of circum-Rodinia subduction system in the late Neoproterozoic. Position and orientation of the Tarim Craton and other major continents are according to [10]. (**b**) Schematic model illustrating the formation of the late Cryogenian granitoids in the northern Tarim Craton. Northward slab rollback of the Paleo-Asian Ocean [17] induced upwelling of asthenosphere, which led to syn-subduction extension and large-scale crustal melting of the upper plate (modified after [93]).

Given the fact that the late Cryogenian magmatism is well-exposed in a linear belt along the northern margin of the Tarim Craton (Figure 1b), we consider that the subduction-related extension was most likely triggered by slab rollback that generally leads to major thermal events along the strike of a subduction zone. The northward rollback of the southward subducting Paleo-Asian Oceanic lithosphere triggered extension in the upper plate and associated upwelling of the asthenosphere (Figure 15b), which consequently caused magma underplating combined with increased temperature, leading to large-scale crustal melting along the northern active margin of the Tarim Craton where the A-type and highly fractionated S-type granitoids were formed as a result of the high thermal gradient.

6.4. Implications for the Position of the Terminal Suture between the Tarim Craton and the Altaids

The position of the terminal suture between the southern Altaids and the Tarim Craton is a key to reconstructing the Paleozoic–Mesozoic tectonic evolution of central Asia. In previous studies, the Atbashi–Inylchek–Kawabulack Fault (Figure 1b) was widely accepted as the terminal suture [94]. Alternatively, our recent study based on geologically and structurally well-investigated tectonic mélanges and provenance analysis of imbricated trench-filled turbidites [52,55,57] indicated that the southernmost boundary of the South Tianshan represents the position of the final suture, which is roughly equivalent to the North Tarim Fault (Figure 1b). However, in this interpretation, the orogen strike extension of the terminal suture was unknown due to the uncertainty of the tectonic nature and affinity of the Ku'erchu area (Figure 1b). The new data obtained in this study can provide a key constraint on this issue.

As shown in Figure 1b, the late Cryogenian–Ediacaran magmatism as a response to the breakup of Rodinia has been reported from several locations (e.g., Quruqtagh and Aksu), representing the youngest magmatic event in the Tarim Craton in the Neoproterozoic. In contrast, no widespread coeval magmatism has been well-documented in the southern Altadis so far. The newly obtained geochronological data in this study indicate that Ediacaran (ca. 640 Ma) magmatism also occurred in the Yeyungou and Ku'erchu areas (Figure 2). As noted earlier, the granites have arc-related geochemical signatures and enriched Nd-Hf isotopic compositions, which are very similar to those of granites in the Tarim Craton. This observation demonstrates that the study area was involved in the breakup of Rodinia as a part of the Tarim Craton in the late Neoproterozoic. Therefore, the presence of the late Cryogenian magmatism in the northern Tarim and its absence in the southern Altaids can provide critical evidence for the position of the terminal suture between them. That is to say, the suture should lie to the north of the Yeyungou and Ku'erchu area as shown in Figure 2.

7. Conclusions

1. LA-ICP-MS zircon U-Pb geochronology reveals that the newly identified late Cryogenian A-type and highly fractionated S-type granites in the northern Tarim Craton were emplaced at ca. 640 Ma. The zircon Hf and whole-rock Sr-Nd isotopic compositions indicate that the granites were mainly generated via the partial melting of mature crustal components of the Tarim Craton, with a minor contribution from the mantle.
2. The arc-related geochemical signatures of the granites, integrated with previously published geological, sedimentological, and structural data, indicate that they formed due to a high-temperature gradient in a syn-subduction extensional setting that was probably induced by the northward slab rollback of the Paleo-Asian Oceanic lithosphere.
3. The presence of late Cryogenian magmatism in the northern Tarim Craton and its absence in the southern Altaids provides critical evidence for the position of the terminal suture between them.

Supplementary Materials: The following supporting information can be downloaded at https://www.mdpi.com/article/10.3390/min13111446/s1. Text S1: Analytical methods; Table S1: Compiled crystallization ages of previously published late Cryogenian-Ediacaran magmatic rocks in the northern Tarim Craton [95–102]; Table S2: Results of LA-ICP-MS U-Pb dating of the late Cryogenian granites in this study; Table S3: Results of Hf isotopes for zircons from the late Cryogenian-Ediacaran granitoids in the northern Tarim Craton; Table S4: Geochemical compositions of the late Cryogenian granites in this study; Table S5: Results of Sr-Nd isotopes for the late Cryogenian granites in this study.

Author Contributions: Conceptualization, T.B. and N.A.; methodology, T.B.; software, T.B.; validation, N.A. and P.H.; formal analysis, T.B.; investigation, T.B., J.G. and Y.T.; resources, N.A.; data curation, T.B.; writing—original draft preparation, T.B.; writing—review and editing, N.A. and P.H.; visualization, T.B.; supervision, N.A.; project administration, N.A.; funding acquisition, N.A. All authors have read and agreed to the published version of the manuscript.

Funding: This study was financially supported by the Key Research and Development Program of Xinjiang Uygur Autonomous Region, China (2022B03015-2) and the National Natural Science Foundation of China (41962013).

Data Availability Statement: The data presented in this study are available in Supplementary Materials.

Acknowledgments: The manuscript benefited from careful reviews and constructive comments from anonymous reviewers.

Conflicts of Interest: The authors declare no conflict of interest.

References

1. Breiter, K. Nearly contemporaneous evolution of the A- and S-type fractionated granites in the Krušné hory/Erzgebirge Mts., Central Europe. *Lithos* **2012**, *151*, 105–121. [CrossRef]
2. Xu, Y.G.; Wang, R.C.; Wang, C.Y.; Robert, L.; Wu, F.Y. Highly fractionated granites and rare-metal mineralization. *Lithos* **2021**, *398–399*, 106262. [CrossRef]
3. Collins, W.J.; Huang, H.; Bowden, P.; Kemp, A. Repeated S-I-A-type granite trilogy in the Lachlan Orogen and geochemical contrasts with A-type granites in Nigeria: Implications for petrogenesis and tectonic discrimination. *Geol. Soc. Lond. Spec. Publ.* **2020**, *491*, 53–76. [CrossRef]
4. Eby, G.N. Chemical subdivision of the A-type granitoids; petrogenetic and tectonic implications. *Geology* **1992**, *20*, 641–644. [CrossRef]
5. Whalen, J.B.; Currie, K.L.; Chappell, B.W. A-type granites: Geochemical characteristics, discrimination and petrogenesis. *Contrib. Miner. Petr.* **1987**, *95*, 407–419. [CrossRef]
6. Sylvester, P.J.; Liegeois, J.P. Post-collisional strongly peraluminous granites. *Lithos* **1998**, *45*, 29–44. [CrossRef]
7. Chen, Y.J.; Chen, B.; Duan, X.X.; Sun, H. Origin of highly fractionated peraluminous granites in South China: Implications for crustal anatexis and evolution. *Lithos* **2021**, *402–403*, 106145. [CrossRef]
8. Qin, Q.; Wang, T.; Huang, H.; Zhang, Z.C.; Tong, Y.; Song, P.; Zhang, J.J. Late Carboniferous and Early Permian garnet-bearing granites in the South Tianshan Belt, NW China: Two Late Paleozoic magmatic events and implications for crustal reworking. *J. Asian Earth Sci.* **2021**, *220*, 104923. [CrossRef]
9. Lu, S.N.; Li, H.K.; Zhang, C.L.; Niu, G.H. Geological and geochronological evidence for the Precambrian evolution of the Tarim Craton and surrounding continental fragments. *Precambrian Res.* **2008**, *160*, 94–107. [CrossRef]
10. Li, Z.X.; Bogdanova, S.V.; Collins, A.S.; Davidson, A.; De Waele, B.; Ernst, R.E.; Fitzsimons, I.C.W.; Fuck, R.A.; Gladkochub, D.P.; Jacobs, J.; et al. Assembly, configuration, and break-up history of Rodinia: A synthesis. *Precambrian Res.* **2008**, *160*, 179–210. [CrossRef]
11. Li, Z.X.; Evans, D.A.D.; Halverson, G.P. Neoproterozoic glaciations in a revised global palaeogeography from the breakup of Rodinia to the assembly of Gondwanaland. *Sediment. Geol.* **2013**, *294*, 219–232. [CrossRef]
12. Tang, Q.Y.; Zhang, Z.W.; Li, C.S.; Wang, Y.L.; Ripley, E.M. Neoproterozoic subduction-related basaltic magmatism in the northern margin of the Tarim Craton: Implications for Rodinia reconstruction. *Precambrian Res.* **2016**, *286*, 370–378. [CrossRef]
13. Zhang, C.L.; Ye, X.T.; Ernst, R.E.; Zhong, Y.; Zhang, J.; Li, H.K.; Long, X.P. Revisiting the Precambrian evolution of the Southwestern Tarim terrane: Implications for its role in Precambrian supercontinents. *Precambrian Res.* **2019**, *324*, 18–31. [CrossRef]
14. Zhao, G.C.; Wang, Y.J.; Huang, B.C.; Dong, Y.P.; Li, S.Z.; Zhang, G.W.; Yu, S. Geological reconstructions of the East Asian blocks; from the breakup of Rodinia to the assembly of Pangea. *Earth-Sci. Rev.* **2018**, *186*, 262–286. [CrossRef]
15. Zhao, P.; Chen, Y.; Zhan, S.; Xu, B.; Faure, M. The Apparent Polar Wander Path of the Tarim block (NW China) since the Neoproterozoic and its implications for a long-term Tarim-Australia connection. *Precambrian Res.* **2014**, *242*, 39–57. [CrossRef]
16. Wu, G.H.; Chu, X.; Tang, M.; Li, W.Y.; Chen, F.K. Distinct tectono-magmatism on the margins of Rodinia and Gondwana. *Earth Planet. Sci. Lett.* **2023**, *609*, 118099. [CrossRef]

17. Ge, R.F.; Zhu, W.B.; Wilde, S.A.; He, J.W.; Cui, X.; Wang, X.; Zheng, B.H. Neoproterozoic to Paleozoic long-lived accretionary orogeny in the northern Tarim Craton. *Tectonics* **2014**, *33*, 302–329. [CrossRef]
18. Ge, R.F.; Zhu, W.B.; Zheng, B.H.; Wu, H.L.; He, J.W.; Zhu, X.Q. Early Pan-African magmatism in the Tarim Craton: Insights from zircon U-Pb-Lu-Hf isotope and geochemistry of granitoids in the Korla area, NW China. *Precambrian Res.* **2012**, *212–213*, 117–138. [CrossRef]
19. He, D.F.; Yuan, H.; Li, D.; Lei, G.L.; Fan, C.; Chang, Q.S.; Ye, M.L. Chronology, geochemistry and tectonic setting of granites at the core of Tugerming anticline, Tarim basin: Indications of paleozoic extensional and compressional cycle at the northern margin of Tarim continental block. *Acta Pet. Sin.* **2011**, *27*, 133–146. (In Chinese with English Abstract)
20. He, J.W.; Zhu, W.B.; Ge, R.F. New age constraints on Neoproterozoic diamicites in Kuruktag, NW China and Precambrian crustal evolution of the Tarim Craton. *Precambrian Res.* **2014**, *241*, 44–60. [CrossRef]
21. He, J.W.; Zhu, W.B.; Ge, R.F.; Zheng, B.H.; Wu, H.L. Detrital zircon U-Pb ages and Hf isotopes of Neoproterozoic strata in the Aksu area, northwestern Tarim Craton: Implications for supercontinent reconstruction and crustal evolution. *Precambrian Res.* **2014**, *254*, 194–209. [CrossRef]
22. Xu, B.; Zou, H.B.; Chen, Y.; He, J.Y.; Wang, Y. The Sugetbrak basalts from northwestern Tarim Block of northwest China: Geochronology, geochemistry and implications for Rodinia breakup and ice age in the Late Neoproterozoic. *Precambrian Res.* **2013**, *236*, 214–226. [CrossRef]
23. Zhu, W.B.; Zhang, Z.Y.; Shu, L.S.; Lu, H.F.; Su, J.B.; Yang, W. SHRIMP U-Pb zircon geochronology of Neoproterozoic Korla mafic dykes in the northern Tarim Block, NW China: Implications for the longlasting breakup process of Rodinia. *J. Geol. Soc. Lond.* **2008**, *165*, 887–890. [CrossRef]
24. Zhu, W.B.; Zheng, B.H.; Shu, L.S.; Ma, D.S.; Wan, J.L.; Zheng, D.W.; Zhang, Z.Y.; Zhu, X.Q. Geochemistry and SHRIMP U-Pb zircon geochronology of the Korla mafic dykes: Constrains on the Neoproterozoic continental breakup in the Tarim Block, northwest China. *J. Asian Earth Sci.* **2011**, *42*, 791–804. [CrossRef]
25. Xiao, Y.; Wu, G.H.; Vandyk, T.M.; You, L.X. Geochronological and geochemical constraints on late Cryogenian to early Ediacaran magmatic rocks on the northern Tarim Craton: Implications for tectonic setting and affinity with Gondwana. *Int. Geol. Rev.* **2019**, *61*, 2100–2117. [CrossRef]
26. Wei, Y.F.; Li, J.B.; Du, H.X.; Deng, Z.J.; Kang, J.W. The significance of the Sinian post-collision peraluminous granites around south margin of the Southwest Tianshan. *Xinjiang Geol.* **2010**, *28*, 242–246. (In Chinese with English Abstract)
27. Wu, H.X.; Zhang, F.Q.; Dilek, Y.; Chen, H.L.; Wang, C.Y.; Lin, X.B.; Cheng, X.G.; Zhu, K.Y. Mid-Neoproterozoic collision of the Tarim Craton with the Yili-Central Tianshan Block towards the final assembly of Supercontinent Rodinia: A new model. *Earth-Sci. Rev.* **2022**, *228*, 103989. [CrossRef]
28. Xu, B.; Xiao, S.H.; Zou, H.B.; Chen, Y.; Li, Z.X.; Song, B.; Liu, D.Y.; Zhou, C.M.; Yuan, X.L. SHRIMP zircon U-Pb age constraints on Neoproterozoic Quruqtagh diamictites in NW China. *Precambrian Res.* **2009**, *168*, 247–258. [CrossRef]
29. Zhang, C.L.; Ye, X.T.; Li, H.K. The latest Neoproterozoic igneous activity on the northern margin of the Tarim Craton. *Geol. Bull. China* **2014**, *33*, 606–613. (In Chinese with English Abstract)
30. Ren, R.; Guan, S.W.; Zhang, S.C.; Wu, L.; Zhang, H.Y. How did the peripheral subduction drive the Rodinia breakup: Constraints from the Neoproterozoic tectonic process in the northern Tarim Craton. *Precambrian Res.* **2020**, *339*, 105612. [CrossRef]
31. Wu, G.H.; Yang, S.A.; Liu, W.; Nance, R.D.; Chen, X.; Wang, Z.C.; Xiao, Y. Switching from advancing to retreating subduction in the Neoproterozoic Tarim Craton, NW China: Implications for Rodinia breakup. *Geosci. Front.* **2021**, *12*, 161–171. [CrossRef]
32. Zhou, X.J.; Tian, W.Z.; Wu, G.H.; Damian Nance, R.; Chen, Y.Q.; Zhao, Y.W.; Yan, W.; Zhang, Y.Q. Geochemistry and U-Pb-Hf zircon systematics of Cryogenian syn-rift magmatic rocks from the subsurface of the Tarim Craton: Implications for subduction-related continental rifting. *Precambrian Res.* **2022**, *377*, 106733. [CrossRef]
33. Ge, R.F.; Zhu, W.B.; Wu, H.L.; Zheng, B.H.; Zhu, X.Q.; He, J.W. The Paleozoic northern margin of the Tarim Craton: Passive or active? *Lithos* **2012**, *142–143*, 1–15. [CrossRef]
34. Guo, R.Q.; Abuduxun, N.; Qin, Q.; Jia, X.L.; Zhu, Z.X.; Wang, K.Z.; Li, Y.P. Geological characteristics and tectonic significance of Silurian granitic intrusions in the northern Tarim craton, Xinjiang. *Geol. Bull. China* **2013**, *32*, 220–238. (In Chinese with English Abstract)
35. Zhang, C.L.; Zou, H.B.; Li, H.K.; Wang, H.Y. Tectonic framework and evolution of the Tarim Block in NW China. *Gondwana Res.* **2013**, *23*, 1306–1315. [CrossRef]
36. Long, X.P.; Yuan, C.; Sun, M.; Kröner, A.; Zhao, G.C.; Wilde, S.; Hu, A.Q. Reworking of the Tarim Craton by underplating of mantle plume-derived magmas: Evidence from Neoproterozoic granitoids in the Kuluketage area, NW China. *Precambrian Res.* **2011**, *187*, 1–14. [CrossRef]
37. Shu, L.S.; Deng, X.L.; Zhu, W.B.; Ma, D.S.; Xiao, W.J. Precambrian tectonic evolution of the Tarim Block, NW China: New geochronological insights from the Quruqtagh domain. *J. Asian Earth Sci.* **2011**, *42*, 774–790. [CrossRef]
38. He, Z.Y.; Zhang, Z.M.; Zong, K.Q.; Dong, X. Paleoproterozoic crustal evolution of the Tarim Craton: Constrained by zircon U-Pb and Hf isotopes of meta-igneous rocks from Korla and Dunhuang. *J. Asian Earth Sci.* **2013**, *78*, 54–70. [CrossRef]
39. Wang, X.D.; Lv, X.B.; Cao, X.F.; Wang, Y.F.; Liu, W. Palaeo-Mesoproterozoic magmatic and metamorphic events from the Kuluketage block, northeast Tarim Craton: Geochronology, geochemistry and implications for evolution of Columbia. *Geol. J.* **2018**, *53*, 120–138. [CrossRef]

40. Ge, R.F.; Zhu, W.B.; Wilde, S.A. Mid-Neoproterozoic (ca. 830–800 Ma) metamorphicP-T paths link Tarim to the circum-Rodinia subduction-accretion system. *Tectonics* **2016**, *35*, 1465–1488. [CrossRef]
41. Lu, Y.Z.; Zhu, W.B.; Ge, R.F.; Zheng, B.H.; He, J.W.; Diao, Z.P. Neoproterozoic active continental margin in the northwestern Tarim Craton: Clues from Neoproterozoic (meta)sedimentary rocks in the Wushi area, northwest China. *Precambrian Res.* **2017**, *298*, 88–106. [CrossRef]
42. Xu, B.; Jian, P.; Zheng, H.F.; Zou, H.B.; Zhang, L.F.; Liu, D.Y. U-Pb zircon geochronology and geochemistry of Neoproterozoic volcanic rocks in the Tarim Block of northwest China: Implications for the breakup of Rodinia supercontinent and Neoproterozoic glaciations. *Precambrian Res.* **2005**, *136*, 107–123. [CrossRef]
43. BGMRXUAR. Regional Geology of Xinjiang Uygur Autonomous Region. *Geol. Publ. House Beijing* **1993**, *657–658*, 732. (In Chinese with English Abstract)
44. Zhang, C.L.; Li, X.H.; Li, Z.X.; Lu, S.N.; Ye, H.M.; Li, H.M. Neoproterozoic ultramafic-mafic-carbonatite complex and granitoids in Quruqtagh of northeastern Tarim Block, western China: Geochronology, geochemistry and tectonic implications. *Precambrian Res.* **2007**, *152*, 149–169. [CrossRef]
45. Zhang, C.L.; Zou, H.B.; Wang, H.Y.; Li, H.K.; Ye, H.M. Multiple phases of the Neoproterozoic igneous activity in Quruqtagh of the northeastern Tarim Block, NW China: Interaction between plate subduction and mantle plume? *Precambrian Res.* **2012**, *222–223*, 488–502. [CrossRef]
46. Li, H.X.; Zhang, Z.C.; Santosh, M.; Wang, Z.C.; Jin, S.K.; Zhang, Q.; Liu, L.H. Ferrodoleritic dykes in the Tarim Craton signal Neoproterozoic breakup of Rodinia supercontinent. *J. Asian Earth Sci.* **2020**, *200*, 104476. [CrossRef]
47. Xiao, W.J.; Windley, B.F.; Allen, M.B.; Han, C.M. Paleozoic multiple accretionary and collisional tectonics of the Chinese Tianshan orogenic collage. *Gondwana Res.* **2013**, *23*, 1316–1341. [CrossRef]
48. Sengör, A.M.C.; Natal'In, B.A.; Sunal, G.; van der Voo, R. The tectonics of the Altaids: Crustal growth during the construction of the continental lithosphere of Central Asia between ∼750 and ∼130 Ma ago. *Annu. Rev. Earth Planet. Sci.* **2018**, *46*, 439–494. [CrossRef]
49. Wilhem, C.; Windley, B.F.; Stampfli, G.M. The Altaids of Central Asia: A tectonic and evolutionary innovative review. *Earth-Sci. Rev.* **2012**, *113*, 303–341. [CrossRef]
50. Long, L.L.; Gao, J.; Klemd, R.; Beier, C.; Qian, Q.; Zhang, X.; Wang, J.B.; Jiang, T. Geochemical and geochronological studies of granitoid rocks from the western Tianshan Orogen: Implications for continental growth in the southwestern Central Asian Orogenic Belt. *Lithos* **2011**, *126*, 321–340. [CrossRef]
51. Qin, Q.; Huang, H.; Wang, T.; Guo, R.; Zhang, Z.; Tong, Y. Relationship of the Tarim Craton to the Central Asian Orogenic Belt: Insights from Devonian intrusions in the northern margin of Tarim Craton, China. *Int. Geol. Rev.* **2016**, *58*, 2007–2028. [CrossRef]
52. Abuduxun, N.; Xiao, W.J.; Windley, B.F.; Chen, Y.C.; Huang, P.; Sang, M.; Li, L.; Liu, X.J. Terminal suturing between the Tarim Craton and the Yili-Central Tianshan arc: Insights from mélange-ocean plate stratigraphy, detrital zircon ages, and provenance of the South Tianshan accretionary complex. *Tectonics* **2021**, *40*, e2021TC006705. [CrossRef]
53. Alexeiev, D.V.; Biske, Y.S.; Wang, B.; Djenchuraeva, A.V.; Getman, O.F.; Aristov, V.A.; Kr Ner, A.; Liu, H.; Zhong, L. Tectono-Stratigraphic framework and Palaeozoic evolution of the Chinese South Tianshan. *Geotectonics* **2015**, *49*, 93–122. [CrossRef]
54. Jiang, T.; Gao, J.; Klemd, R.; Qian, Q.; Zhang, X.; Xiong, X.; Wang, X.; Tan, Z.; Chen, B. Paleozoic ophiolitic mélanges from the South Tianshan Orogen, NW China: Geological, geochemical and geochronological implications for the geodynamic setting. *Tectonophysics* **2014**, *612*, 106–127. [CrossRef]
55. Sang, M.; Xiao, W.J.; Orozbaev, R.; Bakirov, A.; Sakiev, K.; Pak, N.; Ivleva, E.; Zhou, K.; Ao, S.J.; Qiao, Q.Q.; et al. Structural styles and zircon ages of the South Tianshan accretionary complex, Atbashi Ridge, Kyrgyzstan: Insights for the anatomy of ocean plate stratigraphy and accretionary processes. *J. Asian Earth Sci.* **2018**, *153*, 9–41. [CrossRef]
56. Soldner, J.; Oliot, E.; Schulmann, K.; Štípská, P.; Kusbach, V.; Anczkiewicz, R. Metamorphic P-T-t-d evolution of (U)HP metabasites from the South Tianshan accretionary complex (NW China): Implications for rock deformation during exhumation in a subduction channel. *Gondwana Res.* **2017**, *47*, 161–187. [CrossRef]
57. Abuduxun, N.; Windley, B.F.; Xiao, W.J.; Zhang, J.E.; Chen, Y.C.; Huang, P.; Gan, J.M.; Sang, M. Carboniferous tectonic incorporation of a Devonian seamount and oceanic crust into the South Tianshan accretionary orogen in the southern Altaids. *Int. J. Earth Sci.* **2022**, *111*, 2535–2553. [CrossRef]
58. Chen, B.; Long, X.P.; Yuan, C.; Wang, Y.J.; Sun, M.; Xiao, W.J.; Cai, K.D.; Huang, Z.Y. Geochronology and geochemistry of Late Ordovician-Early Devonian gneissic granites in the Kumishi area, northern margin of the South Tianshan Belt: Constraints on subduction process of the South Tianshan Ocean. *J. Asian Earth Sci.* **2015**, *113*, 293–309. [CrossRef]
59. Corfu, F.; Hanchar, J.M.; Hoskin, P.W.O.; Kinny, P.D.; Hanchar, J.M.; Hoskin, P.W.O. Atlas of zircon textures. *Rev. Mineral. Geochem.* **2003**, *53*, 469–500. [CrossRef]
60. Cox, K.G.; Bell, J.D.; Pankhurst, R.J. *The Interpretation of Igneous Rocks*; Allen: London, UK, 1979.
61. Peccerillo, A.; Taylor, S.R. Geochemistry of Eocene calc-alkaline volcanic rocks from the Kastamonu area, northern Turkey. *Contrib. Miner. Petrol.* **1976**, *58*, 63–81. [CrossRef]
62. Maniar, P.D.; Piccoli, P.M. Tectonic discrimination of granitoids. *Geol. Soc. Am. Bull.* **1989**, *101*, 635–643. [CrossRef]
63. Sun, S. Lead isotopic study of young volcanic rocks from mid-ocean ridges, ocean islands and island arcs. *Philos. Trans. R. Soc. Lond. Ser. A Math. Phys. Sci.* **1980**, *297*, 409–445.
64. Bonin, B. A-type granites and related rocks: Evolution of a concept, problems and prospects. *Lithos* **2007**, *97*, 1–29. [CrossRef]

65. Chappell, B.W. Two contrasting granite types. *Pacif. Geol.* **1974**, *8*, 173–174.
66. Chappell, B.W.; Sial, A.N.; Stephens, W.E.; Ferreira, V.P. Aluminium saturation in I-and S-type granites and the characterization of fractionated haplogranites. *Lithos* **1999**, *46*, 535–551. [CrossRef]
67. Collins, W.J.; Beams, S.D.; White, A.J.R.; Chappell, B.W. Nature and origin of A-type granites with particular reference to southeastern Australia. *Contrib. Miner. Petrol.* **1982**, *80*, 189–200. [CrossRef]
68. Eby, G.N.; Woolley, A.R.; Ross, M. The A-type granitoids; a review of their occurrence and chemical characteristics and speculations on their petrogenesis. *Lithos* **1990**, *26*, 115–134. [CrossRef]
69. Regelous, A.; Scharfenberg, L.; De Wall, H. Origin of S-, A- and I-Type Granites: Petrogenetic Evidence from Whole Rock Th/U Ratio Variations. *Minerals* **2021**, *11*, 672. [CrossRef]
70. King, P.L.; White, A.J.R.; Chappell, B.W.; Allen, C.M. Characterization and Origin of Aluminous A-type Granites from the Lachlan Fold Belt, Southeastern Australia. *J. Pet.* **1997**, *38*, 371–391. [CrossRef]
71. Wu, F.Y.; Liu, X.C.; Ji, W.Q.; Wang, J.M.; Yang, L. Highly fractionated granites: Recognition and research. *Sci. China Earth Sci.* **2017**, *60*, 1201–1219. [CrossRef]
72. Ballouard, C.; Poujol, M.; Boulvais, P.; Branquet, Y.; Tartese, R.; Vigneresse, J. Nb-Ta fractionation in peraluminous granites: A marker of the magmatic-hydrothermal transition. *Geology* **2016**, *44*, 231–234. [CrossRef]
73. Mushkin, A.; Navon, O.; Halicz, L.; Hartmann, G.; Stein, M. The petrogenesis of A-type magmas from the Amram Massif, southern Israel. *J. Pet.* **2003**, *44*, 815–832. [CrossRef]
74. Smith, D.R.; Noblett, J.; Wobus, R.A.; Unruh, D.M.; Douglass, J.; Beane, R.; Davis, C.; Goldman, S.; Kay, G.; Gustavson, B.; et al. Petrology and geochemistry of late-stage intrusions of the A-type, mid-Proterozoic Pikes Peak Batholith (central Colorado, USA); implications for petrogenetic models. *Precambrian Res.* **1999**, *98*, 271–305. [CrossRef]
75. Turner, S.P.; Foden, J.D.; Morrison, R.S. Derivation of some A-type magmas by fractionation of basaltic magma: An example from the Padthaway Ridge, South Australia. *Lithos* **1992**, *28*, 151–179. [CrossRef]
76. Clemens, J.D.; Holloway, J.R.; White, A. Origin of an A-type granite; experimental constraints. *Am. Miner.* **1986**, *71*, 317–324.
77. Kemp, A.I.S.; Wormald, R.J.; Whitehouse, M.J.; Price, R.C. Hf isotopes in zircon reveal contrasting sources and crystallization histories for alkaline to peralkaline granites of Temora, southeastern Australia. *Geology* **2005**, *33*, 797–800. [CrossRef]
78. Yang, J.H.; Wu, F.Y.; Chung, S.L.; Wilde, S.A.; Chu, M.F. A hybrid origin for the Qianshan A-type granite, northeast China: Geochemical and Sr-Nd-Hf isotopic evidence. *Lithos* **2006**, *89*, 89–106. [CrossRef]
79. Patiño Douce, A.E. Generation of metaluminous A-type granites by low-pressure melting of calc-alkaline granitoids. *Geology* **1997**, *25*, 743–746. [CrossRef]
80. Litvinovsky, B.A.; Jahn, B.; Zanvilevich, A.N.; Saunders, A.; Poulain, S.; Kuzmin, D.V.; Reichow, M.K.; Titov, A.V. Petrogenesis of syenite-granite suites from the Bryansky Complex (Transbaikalia, Russia); implications for the origin of A-type granitoid magmas. *Chem. Geol.* **2002**, *189*, 105–133. [CrossRef]
81. Wu, F.Y.; Sun, D.Y.; Li, H.M.; Jahn, B.; Wilde, S. A-type granites in northeastern China; age and geochemical constraints on their petrogenesis. *Chem. Geol.* **2002**, *187*, 143–173. [CrossRef]
82. Karsli, O.; Aydin, F.; Uysal, I.; Dokuz, A.; Kumral, M.; Kandemir, R.; Budakoglu, M.; Ketenci, M. Latest Cretaceous "A_2-type" granites in the Sakarya Zone, NE Turkey: Partial melting of mafic lower crust in response to roll-back of Neo-Tethyan oceanic lithosphere. *Lithos* **2018**, *302*, 312–328. [CrossRef]
83. Mao, Q.G.; Xiao, W.J.; Fang, T.H.; Windley, B.F.; Sun, M.; Ao, S.J.; Zhang, J.E.; Huang, X.K. Geochronology, geochemistry and petrogenesis of Early Permian alkaline magmatism in the Eastern Tianshan: Implications for tectonics of the Southern Altaids. *Lithos* **2014**, *190–191*, 37–51. [CrossRef]
84. Pitcher, W.S. Phanerozoic plutonism in the Peruvian Andes. In *Andean Magmatism: Chemical and Isotopic Constraints*; Shiva: Nantwich, UK, 1984; pp. 152–167.
85. Altherr, R.; Holl, A.; Hegner, E.; Langer, C.; Kreuzer, H. High-potassium, calc-alkaline I-type plutonism in the European Variscides: Northern Vosges (France) and northern Schwarzwald (Germany). *Lithos* **2000**, *50*, 51–73. [CrossRef]
86. He, Z.Y.; Klemd, R.; Zhang, Z.M.; Zong, K.Q.; Sun, L.X.; Tian, Z.L.; Huang, B.T. Mesoproterozoic continental arc magmatism and crustal growth in the eastern Central Tianshan arc terrane of the southern Central Asian Orogenic Belt: Geochronological and geochemical evidence. *Lithos* **2015**, *236–237*, 74–89. [CrossRef]
87. Ma, X.X.; Shu, L.S.; Santosh, M.; Li, J.Y. Paleoproterozoic collisional orogeny in Central Tianshan: Assembling the Tarim Block within the Columbia supercontinent. *Precambrian Res.* **2013**, *228*, 1–19. [CrossRef]
88. Su, Y.P.; Zheng, J.P.; Liang, L.L.; Dai, H.K.; Zhao, J.H.; Chen, M.; Ping, X.Q.; Liu, Z.Q.; Wang, J. Derivation of A_1-type granites by partial melting of newly underplated rocks related with the Tarim mantle plume. *Geol. Mag.* **2019**, *156*, 409–429. [CrossRef]
89. Pearce, J.A.; Harris, N.B.W.; Tindle, A.G. Trace element discrimination diagrams for the tectonic interpretation of granitic rocks. *J. Pet.* **1984**, *25*, 956–983. [CrossRef]
90. Chen, H.J.; Chen, Y.J.; Ripley, E.M.; Li, C.S.; Deng, X.H.; Yue, S.W.; Zheng, Z.; Fu, B. Isotope and trace element studies of the Xingdi II mafic-ultramafic complex in the northern rim of the Tarim Craton: Evidence for emplacement in a Neoproterozoic subduction zone. *Lithos* **2017**, *278–281*, 274–284. [CrossRef]
91. Wu, L.; Guan, S.W.; Ren, R.; Wang, X.B.; Yang, H.J.; Jin, J.Q.; Zhu, G.Y. The characteristics of Precambrian sedimentary basin and the distribution of deep source rock: A case study of Tarim Basin in Neoproterozoic and source rocks in Early Cambrian, Western China. *Pet. Explor. Dev.* **2016**, *43*, 988–999. [CrossRef]

92. Sengör, A.M.C.; Burke, K. Relative timing of rifting and volcanism on Earth and its tectonic implications. *Geophys. Res. Lett.* **1978**, *5*, 419–421. [CrossRef]
93. Abuduxun, N.; Xiao, W.; Windley, B.F.; Huang, P.; Yang, H.; Gan, J.; Sang, M.; Liu, X. Early Permian syn-subduction extension in the South Tianshan (NW China): Insights from A-type granitoids in the Southern Altaids. *Front. Earth Sci.* **2022**, *9*, 831677. [CrossRef]
94. Wang, X.S.; Klemd, R.; Gao, J.; Jiang, T.; Li, J.L.; Xue, S.C. Final assembly of the southwestern Central Asian Orogenic Belt as constrained by the evolution of the South Tianshan Orogen: Links with Gondwana and Pangea. *J. Geophys. Res. Solid. Earth* **2018**, *123*, 7361–7388. [CrossRef]
95. Blichert-Toft, J.; Chauvel, C.; Albarede, F. Separation of Hf and Lu for high-precision isotope analysis of rock samples by magnetic sector-multiple collector ICP-MS. *Contrib. Miner. Petrol.* **1997**, *127*, 248–260. [CrossRef]
96. Bouvier, A.; Vervoort, J.D.; Patchett, P.J. The Lu-Hf and Sm-Nd isotopic composition of CHUR: Constraints from unequilibrated chondrites and implications for the bulk composition of terrestrial planets. *Earth Planet. Sci. Lett.* **2008**, *273*, 48–57. [CrossRef]
97. Fisher, C.M.; Vervoort, J.D.; Hanchar, J.M. Guidelines for reporting zircon Hf isotopic data by LA-MC-ICPMS and potential pitfalls in the interpretation of these data. *Chem. Geol.* **2014**, *363*, 125–133. [CrossRef]
98. Griffin, W.L.; Pearson, N.J.; Belousova, E.; Jackson, S.E.; Van Achterbergh, E.; OReilly, S.Y.; Shee, S.R. The Hf isotope composition of cratonic mantle: LAM-MC-ICPMS analysis of zircon megacrysts in kimberlites. *Geochim. Cosmochim. Acta* **2000**, *64*, 133–147. [CrossRef]
99. Liu, Y.S.; Gao, S.; Hu, Z.C.; Gao, C.G.; Zong, K.Q.; Wang, D.B. Continental and oceanic crust recycling-induced melt-peridotite interactions in the Trans-North China Orogen: U-Pb dating, Hf isotopes and trace elements in zircons from mantle xenoliths. *J. Pet.* **2010**, *51*, 537–571. [CrossRef]
100. Ludwig, K.R. *User's Manual for Isoplot/EX, Version 3.00: A Geochronological Toolkit Microsoft Excel*; Stanford University Libraries: Stanford, CA, USA, 2003; Volume 4, p. 71.
101. Paton, C.; Woodhead, J.D.; Hellstrom, J.C.; Hergt, J.M.; Greig, A.; Maas, R. Improved laser ablation U-Pb zircon geochronology through robust downhole fractionation correction. *Geochem. Geophys. Geosyst.* **2010**, *11*, 1–36. [CrossRef]
102. Wiedenbeck, M.; Alle, P.; Corfu, F.; Griffin, W.L.; Meier, M.; Oberli, F.; Von Quadt, A.; Roddick, J.C.; Spiegel, W. Three natural zircon standards for U-Th-Pb, Lu-Hf, trace element and REE analyses. *Geostand. Newsl.* **1995**, *19*, 1–23. [CrossRef]